Diffraction dissociation of photons on hydrogen

T. J. Chapin, R. L. Cool, K. Goulianos, K. A. Jenkins,* J. P. Silverman,* G. R. Snow, H. Sticker, and S. N. White
The Rockefeller University, New York, New York 10021

Yue Hua Chou
Institute for High Energy Physics, Beijing, The People's Republic of China
(Received 29 May 1984)

We report results from a measurement of the inclusive diffraction dissociation of photons on hydrogen, $\gamma p \to Xp$, in the range $75 < p_\gamma < 148$ GeV/c, $0.02 < |t| < 0.1$ (GeV/c)^2, and $M_X^2/s < 0.1$. Our data show an exponential t dependence and a dominant $1/M_X^2$ behavior for $M_X^2 > 4$ GeV^2. We test the finite-mass sum rule and, by comparing γp with $\pi^- p$ data obtained in the same apparatus, we test factorization.

I. INTRODUCTION

In an experiment performed at Fermilab, E-612, we measured the inclusive diffraction-dissociation cross section $d^2\sigma/dt\,dM_X^2$ of photons incident on protons,

$$\gamma + p \to X + p \ , \tag{1}$$

in the kinematic range $75 < p_\gamma < 148$ GeV/c, $0.02 < |t| < 0.1$ (GeV/c)^2, and $M_X^2/s < 0.1$. As a control experiment, we also measured, in the same apparatus, the pion diffraction-dissociation cross section,

$$\pi^- + p \to X + p \ , \tag{2}$$

at 100 GeV/c. Pion dissociation has been measured previously;[1] this experiment represents the first measurement of the inclusive diffraction dissociation of photons at high energies.

For hadron dissociation, $hp \to Xp$, it is known[2] that the differential cross sections are exponential in t and vary as $1/M_X^2$. This behavior is described well by a simple triple-Pomeron Regge amplitude. Assuming factorization of the diffractive vertex in such an amplitude, the diffractive cross sections of different hadrons dissociating on protons should scale to the corresponding total cross sections. This scaling has been checked experimentally[1] for $h = \pi^\pm, K^\pm, p^\pm$ and has been found to hold within the experimental accuracy of $\sim 10\%$. In addition to yielding the factorization result, the triple-Pomeron amplitude satisfies the finite-mass sum rule (FMSR) which is based on analyticity and crossing symmetry.[3] In terms of the cross-symmetric variable $\nu = M_X^2 - M_h^2 - t$, where M_h is the mass of the incident hadron, the FMSR states that the extrapolation of the high-ν behavior of the cross section $\nu(d^2\sigma/dt\,d\nu)$ into the low-ν "resonance region" represents the average behavior of the "resonances," including elastic scattering for which $\nu = |t|$. Quantitatively,

$$|t|\frac{d\sigma_{\rm el}}{dt} + \int_0^{\nu'} \nu \frac{d^2\sigma}{dt\,d\nu} d\nu = \int_0^{\nu'} \nu \left[\frac{d^2\sigma}{dt\,d\nu}\right]_{\text{fit for } \nu > \nu'} d\nu \ . \tag{3}$$

Here, the value of ν' must lie beyond the resonance region but is otherwise arbitrary. Equation (3) was checked for $pp \to Xp$ (derived from data on $pd \to Xd$) and was found to hold to an experimental accuracy of a few percent.[4] As $|t| \to 0$, the elastic contribution to the left-hand side of Eq. (3) vanishes, but is compensated by a low-mass enhancement which becomes more prominent as t decreases. For $pp \to Xp$, this enhancement is the $N^*(1400)$. For pion and kaon dissociation, the analogous role is played by the A_1 and Q_1 enhancements, respectively.

The hadronic interaction of the photon is described fairly well by the vector-meson-dominance model (VDM).[5] In its simplest form, this model assumes that a photon interacts hadronically by converting into a virtual vector meson (ρ,ω,ϕ) prior to the interaction. The coherent photoproduction of vector mesons is then described as an elastic-scattering process. Diffractive and total cross sections originate from these vector-meson interactions and therefore the diffraction dissociation of the photon is expected to exhibit the properties of hadronic dissociation: exponential t dependence, $1/M_X^2$ behavior, and factorization. However, the way the FMSR is to be applied in this model is somewhat unclear. The interpretation of the coherent photoproduction of a vector meson as elastic scattering would suggest naively that one should use $\nu = M_X^2 - M_V^2 - t$, where M_V is the mass of the vector meson, for the cross-symmetric variable in Eq. (3). On the other hand, in a strict application of the FMSR for an incident particle of zero mass one should use $\nu = M_X^2 - t$. The result is very sensitive to the choice of this variable and therefore it provides a test of the interpretation of the VDM.

II. METHOD AND APPARATUS

The experiment was performed in the tagged photon beam at Fermilab. The photons were obtained from an 148-GeV/c electron beam incident on a tungsten target of 0.2 radiation lengths. The energy of the photons was determined to $\pm 2\%$ by measuring the momentum of the radiating electrons which were deflected out of the beam

by a bending magnet and then impinged upon a fine-grained hodoscope of scintillation counters followed by electromagnetic shower counters. Consistency between the magnetic bending and the pulse height in the shower counters was used to eliminate background. Typically, the photon beam contained $\sim 1\times 10^6$ tagged photons per pulse in the energy range $75 < E_\gamma < 148$ GeV. Since the bremsstrahlung energy spectrum varies as $1/E$, the mean energy of the photons was about 100 GeV. The acceptable photon flux was limited by the rate capability of our detector. Double photon production in the radiator was tagged by a total absorption counter which, placed in the photon beam downstream of our apparatus, measured the total energy of the noninteracting photons. A pion beam was formed by intercepting the secondary neutral beam,

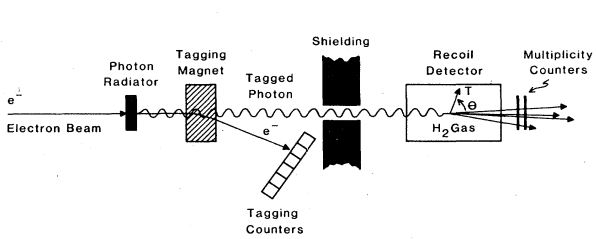

FIG. 1. Experimental arrangement.

which normally created the electrons, with a 10-cm-thick lead target. An electromagnetic halo accompanying the beam limited the acceptable flux of pions to $\sim 5\times 10^4$ per pulse. The pulse-repetition period of the accelerator was

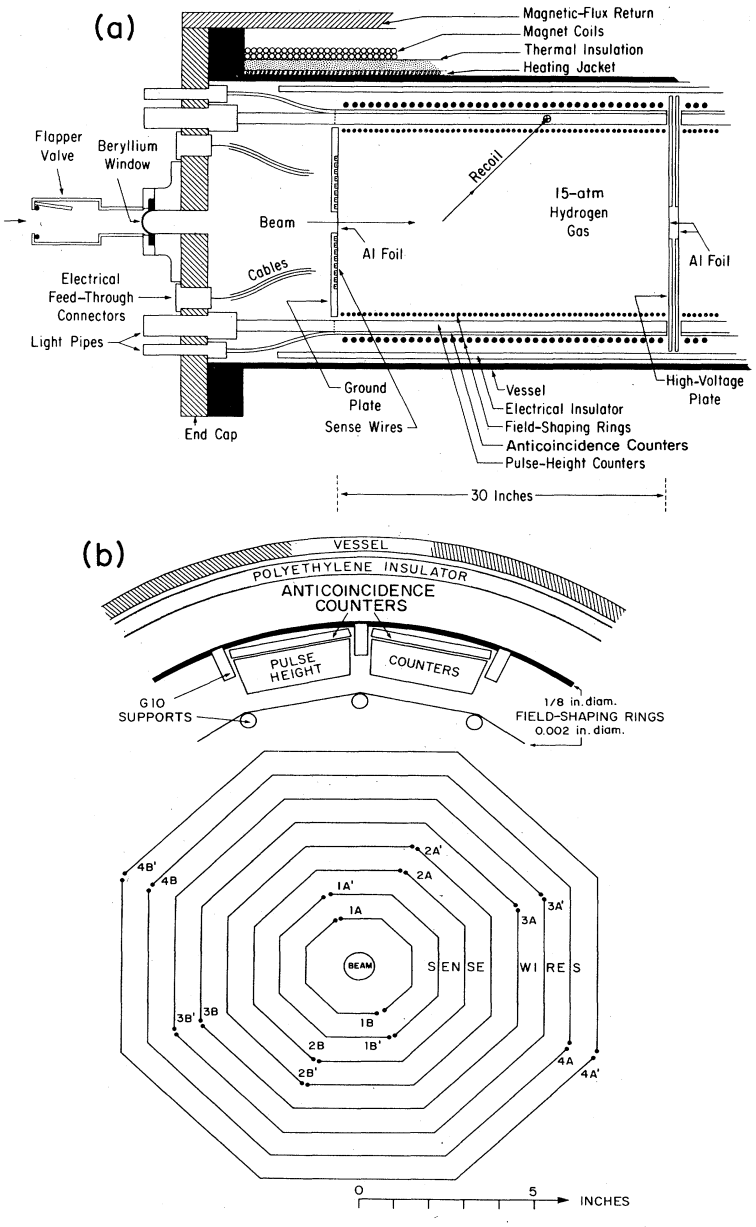

FIG. 2. Apparatus. (a) Plan view; (b) cross-sectional view showing sense-wire and counter arrangement.

~ 10 sec and the beam spill time ~ 1 sec.

The experimental technique consisted of measuring the kinetic energy and polar angle of recoil protons in the range $10 < T < 50$ MeV and $45° < \theta < 90°$. The variables t and M_X^2 were then determined from T, θ, and p_0, the momentum of the beam particle, using the equations

$$t = -2M_p T \,, \tag{4}$$

$$M_X^2 = M_0^2 + 2p_0\sqrt{|t|}\,(\cos\theta - \sqrt{|t|}/2M_p) \,, \tag{5}$$

where M_p is the mass of the recoil proton and M_0 the mass of the incident particle.

The experimental arrangement is shown in Fig. 1. The apparatus, TREAD (the recoil energy and angle detector), shown in Fig. 2, was described in detail in a previous publication.[6] It was a time-projection chamber (TPC) filled with high-pressure (15-atm) hydrogen gas that served both as the target and as the drift medium for the ionization tracks created by recoil protons. It consisted of two cylindrical drift regions in tandem, each 45 cm in diameter and 75 cm long. The beam entered the TPC along the axis of the cylinder through a 0.75-mm-thick, 5-cm-diam beryllium window and excited through a 2-mm-thick, 20-cm-diam aluminum window. The ionization from recoil protons drifted along axial electric field lines toward the end plates where eight octagonal concentric sense wires sampled different parts of the track. The polar angle θ was determined from the differences in the arrival times recorded by successive wires. A conventional solenoidal magnet provided a 1.5-kG axial magnetic field whose purpose was to confine low-energy Compton electrons in a region around the beam and thus prevent them from entering the active area of the TPC and overloading the system. The effect of this field on the recoil protons was negligible. The dissociation products exited through the aluminum window, whereupon their charged multiplicity was determined by measuring the pulse height in two successive scintillation counters. This technique was used previously[7] by some members of this group in a hadron experiment, E-396, performed at Fermilab's meson laboratory. The energy of the recoil protons was determined by stopping them in 75-cm-long$\times$7.6-cm-wide$\times$2.9-cm-thick plastic scintillation counters located inside the pressure vessel. Particles that penetrated through these counters were detected by 6-mm-thick anticoincidence counters. The energy loss in the hydrogen gas, dE/dx, was obtained from the pulse heights of the sense-wire signals. Recoiling protons were identified from the product $T(dE/dx)$ which is proportional to the mass of the recoil particle.

The pulse-height counters were calibrated with cosmic rays and with muons from the production target that traversed the entire length (75 cm) of the counters. Stability was monitored by continuously recording the pulse height from ^{241}Am α sources embedded in NaI and mounted at the end of each counter. Light production in the scintillator was converted to energy loss following a procedure described in a previous publication.[8] The resolution in the measurement of the kinetic energy was about 1 MeV, resulting in $\sigma_t = 0.002$ (GeV/c)^2. The resolution in the measurement of θ was $\sigma_\theta = 5.5$ mrad, with approximately equal contributions from multiple Coulomb scattering and distortions in the TPC.[9] With the beam momentum measured to $\pm 2\%$, as mentioned previously, the mass resolution at 100 GeV/c is then $\sigma(M_X^2) = 0.3$ GeV^2. The determination of the mass of the recoil proton from T and dE/dx was limited by the dE/dx resolution which was about $\pm 30\%$ per wire. A measurement from 4 wires resulted in $\sigma(dE/dx)$, and hence in $\sigma(M_{\text{recoil}}/M_{\text{proton}})$, of about 15%.

The trigger consisted of two levels, "fast" and "slow." The fast level required a coincidence between a tagged photon and a pulse-height counter, in anticoincidence with the downstream total absorption counter mentioned previously. The purpose of this counter was to veto events for which only one of two photons produced in the radiator interacted in the apparatus. A scintillation counter with a hole for the beam was positioned in front of the apparatus and placed in anticoincidence in order to veto events with muons entering the TPC. The fast trigger opened a 180-μsec gate (the length of the maximum drift time in the TPC) within which the slow trigger, incorporating sense wire logic, was required. The sense wire logic consisted essentially of a time coincidence of sense wires corresponding to tracks with polar angles from 45° to 135°. The slow logic also controlled the timing and multiplexing of sample-and-hold circuits used to record dE/dx information.

III. DATA REDUCTION

About 7×10^6 photon and 7×10^5 π^- events were recorded. Of these, 9.9×10^4 photon and 4.6×10^4 pion events contained "good" recoil tracks with at least six out of the eight sense wires firing. The remaining events were mostly due to accidental coincidences of Compton electrons in the chamber with beam associated pulses in the counters. Figure 3 shows a scatter plot of the recoil kinetic energy plotted against dE/dx for photon data that had "good" tracks. The prominent band represents recoil protons. Quantitatively, the number of events containing recoil protons was extracted from histograms of the prod-

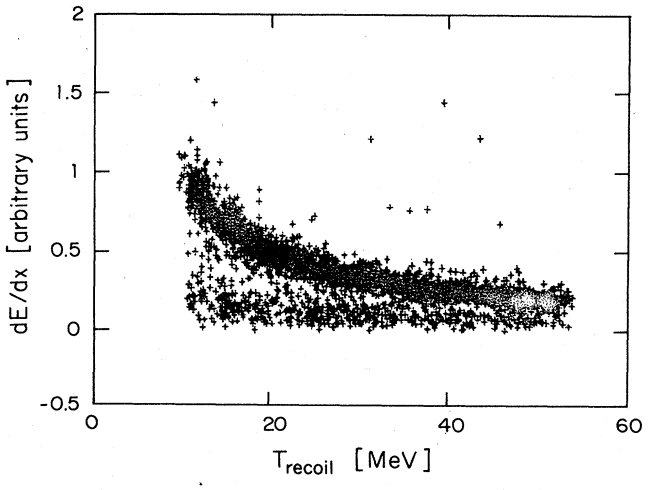

FIG. 3. Recoil-particle energy loss dE/dx versus kinetic energy. The prominent band represents recoil photons.

uct $T(dE/dx)$ which, as mentioned previously, is proportional to the mass of the recoil particle. Figure 4 shows examples of such histograms. In the top part of the figure, the average of the pulse heights measured by five independent wires was used as dE/dx. The fit represents a Landau distribution. The "Landau tail" can be reduced by discarding the two largest of the five measured pulse heights and plotting the average of the remaining three. This results in a narrower, more symmetric distribution, as shown in Fig. 4(b). Using events with good tracks, histograms like those of Fig. 4(b) were made for every M_X^2 and t bin. The number of events with good recoil protons in each bin was then determined by fitting these histograms, obtaining the standard deviation σ from the fits and retaining the events within -2σ and $+2.5\sigma$ from $M/M_p=1$. The background contamination in the number of the good events within each bin is estimated to be $\leq 2\%$. The analysis discussed below is based on 9000 photon and 9200 π^- accepted events.

IV. ANALYSIS

The data were corrected for detection efficiency and normalized by means of the elastic-scattering peaks (in the case of the photon, the ρ peak will be referred to as "elastic"). The separation of the elastic from the inelastic events was facilitated by making use of the charged multiplicity of the events as recorded by the multiplicity counters. In this section we discuss the corrections to the data, the analysis of the charged multiplicity distribution, the extraction of the elastic events and the normalization.

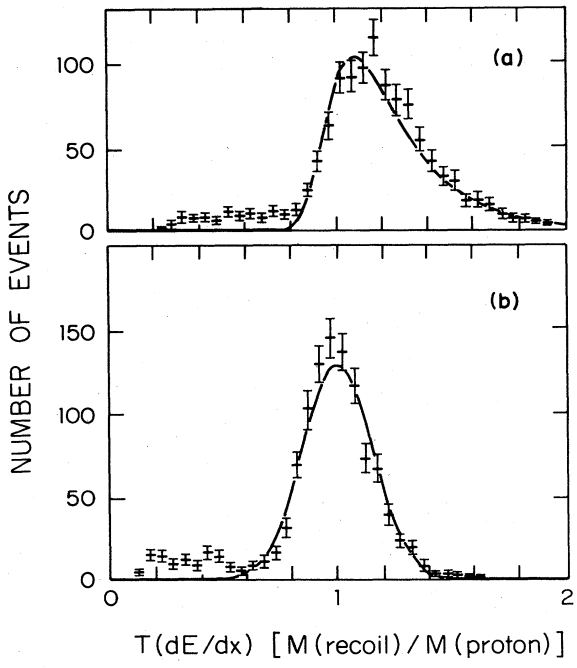

FIG. 4. Recoil-particle energy loss dE/dx times kinetic energy T. The product $T(dE/dx)$ is proportional to the mass of the recoil particle. The position of the peak is normalized to unity so that the abscissa represents M(recoil)/M(proton). (a) dE/dx was obtained as the average of the pulse heights of fives wires; (b) dE/dx here is the average over the remaining three wires after the two largest of the five pulse heights were discarded.

A. Corrections

The largest correction to the data is due to the geometric acceptance of the apparatus. Since the data are normalized through the elastic peaks, only the relative acceptance for events in different (M_X^2,t,p_0) bins is relevant. The acceptance is a simple analytic function of θ, the recoil polar angle. The target length available for an event varies with θ according to $L(\theta)=L-R\cot\theta$, where L is the length of a TPC section and R the radius to the pulse-height counters. For our apparatus, $L=30$ inches and $R=9$ inches (see Fig. 2). The acceptance,

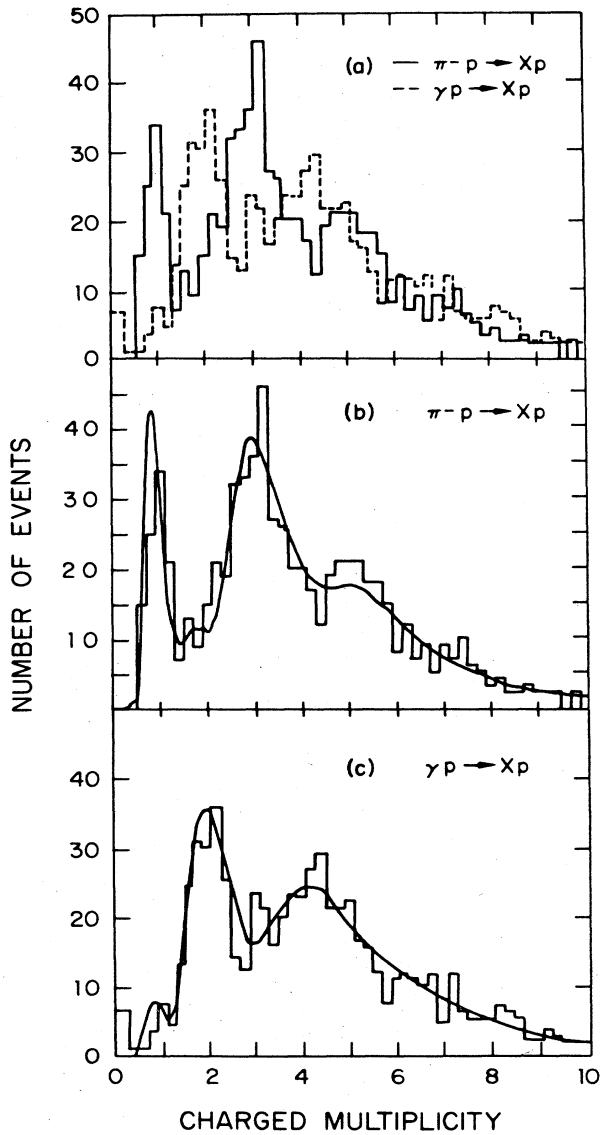

FIG. 5. Charged-particle multiplicity of the diffractive state X for $\pi^-(\gamma)+p\to X+p$ in the mass range $4<M_X^2<10$ GeV^2. The curves represent calculations based on Eq. (6) in the text. The histograms for π^- and γ multiplicities contain equal number of events.

which is proportional to the available target length, is therefore given by $L(\theta)/L = 1 - 0.30\cot\theta$. For our range of polar angles, $45° < \theta < 90°$, the acceptance varies from 78% to 100%.

The data also have to be corrected for nuclear interactions of the recoil protons in the scintillator. This t-dependent effect is $<2\%$ and was taken into account only in the elastic t distributions.

B. Charged multiplicities

The charged multiplicity of the events was determined from the pulse height in the "multiplicity counters." These were two scintillation counters mounted, one behind the other, outside of TREAD at a distance of 1.6 m downstream from its center. The $10.5 \times 10.5 \times \frac{1}{8}$-in. scintillators were optically isolated from each other and viewed by separate phototubes. They covered approximately 94% of the solid angle in the rest frame of a 2-GeV particle created with 100-GeV/c momentum at the center of TREAD.

The multiplicity counters were cross-calibrated with single electrons, electron pairs and the data themselves. For each event, the larger of the normalized pulse heights measured by the two counters was discarded. This reduced the Landau tail, so that the remaining pulse height is a more direct measure of charged multiplicity. A pulse-height spectrum for events in the region $4 < M_X{}^2 < 10$ GeV^2, both from $\pi^- p \to Xp$ and $\gamma p \to Xp$, is shown in Fig. 5. Taking into account the fact that charge conservation restricts the photon and π^- charged multiplicities to even and odd numbers, respectively, the two spectra look similar. This behavior is consistent with the universality of charged multiplicity distributions observed in hadron-induced reactions.[10]

More quantitatively, it was found previously[7,10] that the charged multiplicity distribution of the "decay" products of a hadronic mass M has a mean value $n_0 = 2M^{1/2}$ (M in GeV) and is represented well by a Gaussian function with a width $D = n_0/2$. The normalized probability distribution of the charged multiplicity n is thus given by

$$P_n = \frac{2}{\sqrt{2\pi}D}\exp[-(n-n_0)^2/2D^2]\,,$$
$$n_0 = 2M^{1/2}\ (M \text{ in GeV})\,, \tag{6}$$
$$D = n_0/2\,.$$

Anticipating our result that in the region $4 < M_X{}^2 < 10$ GeV^2 the diffractive cross sections for $\pi^-(\gamma) + p \to X + p$ vary as $1/M_X{}^2$, and using this information in conjunction with the above multiplicity law, we have calculated the curves which are superimposed on the data in Fig. 5. The good agreement between the calculation and the data justifies using the calculation in the manner described below to carry out the extrapolation of the inelastic mass distributions into the region under the elastic peaks.

C. Extraction of elastic events

Figure 6 shows a mass distribution for photon data. Because of the finite resolution in the measurement of $M_X{}^2$, there is significant overlap between the "elastic" ρ peak and the inelastic events. Since the shape of the inelastic mass distribution is not known *a priori*, the extrapolation of the high-mass data into the region under the "elastic" peak cannot be carried out directly. Instead, we use a procedure based on the charged multiplicity of the

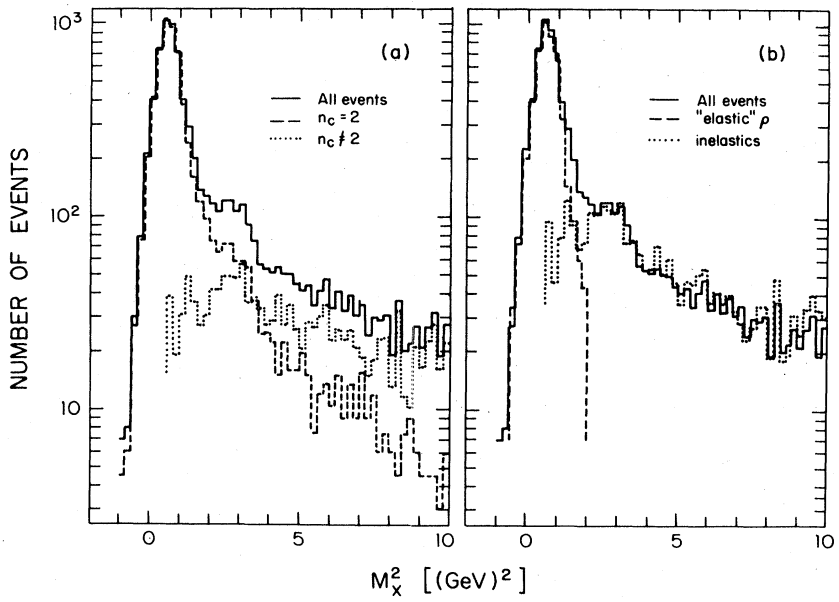

FIG. 6. Extraction of "elastic" events from $\gamma p \to Xp$. (a) The solid line histogram represents the photon data in the energy bin 75–148 GeV; partial histograms for data with charged multiplicity $n_c = 2$ and $n_c \neq 2$ are represented by the dashed and dotted lines. (b) "Elastic" and inelastic events; the elastic events were obtained by correcting the $n_c \neq 2$ histogram of inelastic events for the missing events of multiplicity $n_c = 2$ as explained in the text, and subtracting it from the histogram of all the events.

events (Fig. 5) and the multiplicity distributions described previously [Eq. (6)].

For the photon data only even multiplicities are allowed and therefore a cut requiring $1.5 < n < 2.5$ rejects efficiently events with charged multiplicity $n \neq 2$. The events retained within the cut are mostly due to $\rho^0 \to \pi^+\pi^-$, but they also include the $n=2$ component of the dissociation of higher diffractive masses. However, because of the Landau tail in the pulse height distributions, this cut rejects some events with charged multiplicity of 2. These events may be regained statistically by normalizing the peak of the $n=2$ distribution to the ρ peak in the uncut data. Figure 6(a) shows the $n=2$ spectrum obtained in this manner. Subtracting this spectrum from the overall mass distribution yields the $n \neq 2$ inelastic spectrum, also shown in Fig. 6(a). We now use the multiplicity law, Eq. (6), to correct the inelastic spectrum for the missing $n=2$ multiplications. The result is shown in Fig. 6(b) along with its complement to the overall distribution which now represents the elastic ρ signal. This procedure was applied at each t bin. The same method, but with a multiplicity cut around $n=1$ instead of $n=2$, was used to extract the elastic events from the pion data.

D. Normalization

In principle, the normalization of the data could be determined from the event rates. However, uncertainties in beam intensity, triggering efficiency, dead time, solid angle, and event reconstruction losses limited the accuracy of such a determination to $\sim 30\%$. For this reason, the data were normalized through the elastic events. In the pion case, the elastic data were fitted to the function $d\sigma/dt = A \exp(bt)$ and the constant A was scaled to the optical point,

$$\frac{d\sigma}{dt}(t=0) = \frac{\sigma_T{}^2(1+\rho^2)}{16\pi} ,$$

where σ_T is the total cross section and ρ is the ratio of the real to the imaginary part of the forward scattering amplitude. We set $\rho = 0$, which leads to an uncertainty in A of $< 1\%$, and used the value of 24.0 mb for the total cross section at 100 GeV/c.[11] In the photon case, the normalization was obtained by scaling the number of our elastic events to the normalized photoproduction cross sections of Callahan *et al.*,[12] taking into account the small admixture of ω and ϕ events under the peak. The net correction to the normalization arising from the nonresonant Drell-Söding term, discussed in Sec. V A, is negligible when averaged over our t range. Our estimated normalization accuracy is $\pm 10\%$ for the pion data and $\pm 13\%$ for the proton data.

V. RESULTS

The normalized differential cross sections are presented in Tables I—IV and plotted in Figs. 8 to 13. The energy

TABLE I. Differential cross sections $d\sigma/dt$ and fits to the form Ae^{bt}.

	$\pi^- + p \to X + p$ at 100 GeV/c [mb(GeV/c)$^{-2}$]				
t value [(GeV/c)^2] \ $M_X{}^2$ (GeV^2)	Elastic	0.6—1.6[a]	1.0—3.0	3.0—5.0	5.0—9.0
0.020—0.036	25.6±1.1		5.17±0.29	1.87±0.17	1.82±0.17
0.036—0.052	19.6±1.1		4.16±0.26	1.69±0.16	1.68±0.16
0.052—0.068	18.7±0.9		3.54±0.24	1.34±0.15	1.76±0.17
0.068—0.084	15.8±0.9		3.75±0.24	1.50±0.15	1.33±0.15
0.084—0.100	12.9±0.8		3.53±0.24	1.42±0.15	1.41±0.15
A [mb(GeV/c)$^{-2}$]	32.73		5.59±0.45	2.01±0.25	2.09±0.26
b [(GeV/c)$^{-2}$]	9.9±1.0	13.7±2.0	5.8±1.3	4.2±2.0	4.7±2.0
χ^2/DF (3 DF)	1.32	1.10	2.27	0.93	0.67
	$\gamma + p \to X + p$ at 75—148 GeV/c [μb(GeV/c)$^{-2}$]				
t value [(GeV/c)^2] \ $M_X{}^2$ (GeV^2)	ρ peak	1.2—2.0[a]	2.0—3.0	3.0—5.0	5.0—9.0
0.020—0.036	88.0±4.1		8.57±0.74	9.92±0.80	11.50±0.86
0.036—0.052	76.1±3.8		9.47±0.78	9.92±0.80	10.24±0.81
0.052—0.068	61.4±3.4		8.37±0.73	10.5±0.82	8.50±0.74
0.068—0.084	53.3±3.2		7.80±0.71	8.37±0.73	8.18±0.73
0.084—0.100	45.0±1.1		6.18±0.63	7.15±0.68	9.92±0.80
A [μb(GeV/c)$^{-2}$]	119.1		10.8±1.1	12.1±1.2	11.9±1.2
b [(GeV/c)$^{-2}$]	10.6±1.0	3.7±1.7	4.2±1.4	6.3±1.3	5.1±1.3
χ^2/DF (3 DF)	0.13	0.11	1.23	1.33	2.00

[a]Includes only events with charged multiplicity $n_c \neq 1$ for π^- and $n_c \neq 2$ for γ.

TABLE II. Inelastic differential cross sections $d^2\sigma/dt\,dM_X^2$ at $t=-0.05$ (GeV/c)^2 for $\pi^- p \to Xp$ at 100 GeV/c and $\gamma p \to Xp$ from 75 to 148 GeV/c [in mb (GeV/c)$^{-2}$(GeV)$^{-2}$ and μb (GeV/c)$^{-2}$(GeV)$^{-2}$, respectively]. The $\pi^- p$ elastic and ρ signals were subtracted from the data as described in the text.

M_X^2 (GeV^2)	Beam particle and momentum (GeV/c)			
	π^- (100)	γ (75—100)	γ (100—148)	γ (75—148)
0.0—0.2	0.23 ±0.99			
0.2—0.4	0.38 ±0.74			
0.4—0.6	1.59 ±0.47			
0.6—0.8	2.75 ±0.32	2.42±4.40	0.00±3.60	0.97±2.82
0.8—1.0	2.45 ±0.25	6.61±2.57	1.97±2.21	4.23±1.68
1.0—1.2	3.18 ±0.26	6.05±1.92	2.39±1.71	3.92±1.28
1.2—1.4	3.20 ±0.24	9.65±1.53	8.71±1.49	8.96±1.07
1.4—1.6	2.77 ±0.24	10.05±1.27	9.58±1.25	9.73±0.89
1.6—1.8	2.38 ±0.21	8.42±1.09	7.75±1.02	8.06±0.74
1.8—2.0	2.01 ±0.19	7.98±1.04	8.09±1.00	8.03±0.72
2.0—2.2	1.79 ±0.18	7.10±0.98	7.64±0.97	7.37±0.69
2.2—2.4	1.36 ±0.16	7.12±0.98	6.71±0.90	6.89±0.66
2.4—2.6	1.29 ±0.15	7.80±1.02	7.57±0.96	7.67±0.70
2.6—2.8	1.36 ±0.16	8.35±1.06	7.10±0.93	7.68±0.70
2.8—3.0	0.90 ±0.13	5.66±0.87	7.84±0.98	6.79±0.66
3.0—3.2	1.13 ±0.14	8.64±1.08	6.26±0.87	7.38±0.69
3.2—3.4	1.12 ±0.14	6.22±0.92	5.53±0.82	5.85±0.61
3.4—3.6	0.80 ±0.12	4.33±0.77	5.17±0.80	4.76±0.55
3.6—3.8	0.72 ±0.11	4.21±0.76	3.21±0.63	3.67±0.49
3.8—4.0	0.82 ±0.12	3.53±0.69	3.33±0.64	3.42±0.47
4.0—5.0	0.69 ±0.05	3.44±0.31	3.05±0.27	3.23±0.20
5.0—6.0	0.54 ±0.04	2.94±0.28	2.50±0.25	2.70±0.19
6.0—7.0	0.425±0.040	2.58±0.27	2.06±0.23	2.30±0.17
7.0—8.0	0.391±0.038	1.87±0.23	2.08±0.23	1.98±0.16
8.0—9.0	0.282±0.033	1.89±0.23	1.48±0.19	1.67±0.15
9.0—10.0	0.269±0.032	1.90±0.23	1.55±0.20	1.71±0.15
10.0—12.0	0.251±0.022	1.76±0.16	1.22±0.13	1.47±0.10
12.0—14.0	0.211±0.020	1.27±0.14	1.26±0.13	1.27±0.09
14.0—16.0	0.184±0.019	1.31±0.14	1.22±0.13	1.26±0.09
16.0—18.0	0.206±0.021	1.30±0.14	1.11±0.12	1.20±0.09

spectrum of the photons is shown in Fig. 7. For each event, the energy of the interacting photon was obtained by subtracting the energy recorded by the downstream total absorption counter from the energy given by the tagging system. Since the lowest tagged photon energy was 65 GeV, the events with energy less than 65 GeV are

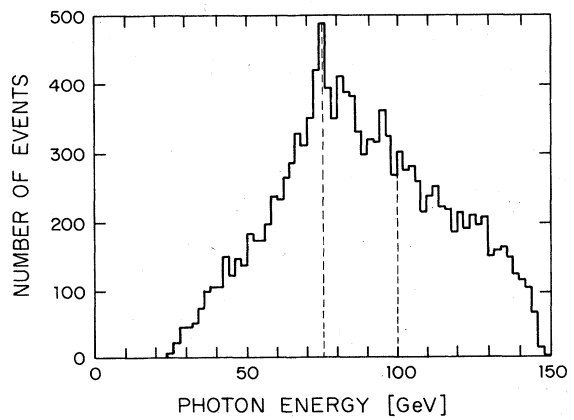

FIG. 7. The energy spectrum of the photon data. The vertical dashed lines define the energy regions in which the data were binned.

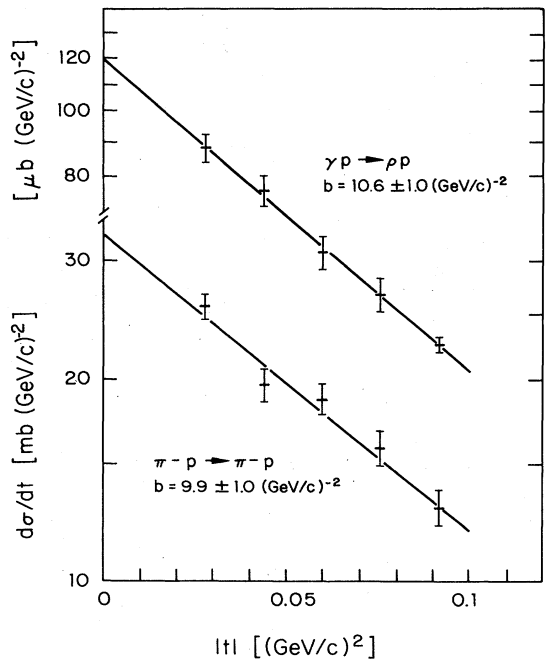

FIG. 8. Elastic differential cross sections as a function of t. The lines represent fits to the form $d\sigma/dt = Ae^{bt}$.

TABLE III. Differential cross sections as in Table II including the $\pi^- p$ elastic and ρ signals. The data beyond $M_X{}^2=2$ GeV^2 are not shown here as they are identical to those in Table II. The cross sections extend to negative values of $M_X{}^2$ due to the finite resolution of the experiment.

$M_X{}^2$ (GeV^2)	Beam particle and momentum (GeV/c)			
	π^- (100)	γ (75—100)	γ (100—148)	γ (75—148)
−5.0—(−4.8)	0.017±0.017	0	0.12±0.12	0.06±0.06
−4.8—(−4.6)	0.017±0.017	0	0	0
−4.6—(−4.4)	0.017±0.017	0.13±0.13	0	0.06±0.06
−4.4—(−4.2)	0	0	0	0
−4.2—(−4.0)	0	0	0.24±0.16	0.12±0.09
−4.0—(−3.8)	0	0	0	0
−3.8—(−3.6)	0.017±0.017	0	0	0
−3.6—(−3.4)	0	0.13±0.13	0.12±0.12	0.12±0.09
−3.4—(−3.2)	0.000±0.017	0	0	0
−3.2—(−3.0)	0.017±0.017	0	0.12±0.12	0.06±0.06
−3.0—(−2.8)	0	0.13±0.13	0	0.06±0.06
−2.8—(−2.6)	0.035±0.025	0.13±0.13	0.12±0.12	0.12±0.09
−2.6—(−2.4)	0	0	0	0
−2.4—(−2.2)	0	0.13±0.13	0.24±0.16	0.18±0.11
−2.2—(−2.0)	0.052±0.030	0	0	0
−2.0—(−1.8)	0.017±0.017	0	0.12±0.12	0.06±0.06
−1.8—(−1.6)	0.035±0.025	0.13±0.13	0	0.06±0.06
−1.6—(−1.4)	0.035±0.025	0.26±0.18	0.24±0.16	0.24±0.12
−1.4—(−1.2)	0.122±0.046	0.13±0.13	0.48±0.24	0.30±0.14
−1.2—(−1.0)	0.192±0.058	0.39±0.23	0.36±0.21	0.36±0.15
−1.0—(−0.8)	0.54 ±0.10	0.26±0.19	0.60±0.27	0.44±0.17
−0.8—(−0.6)	1.77 ±0.18	0.13±0.13	0.84±0.32	0.50±0.18
−0.6—(−0.4)	6.28 ±0.33	0.66±0.29	2.63±0.56	1.69±0.33
−0.4—(−0.2)	17.0 ±0.55	3.82±0.71	6.00±0.85	4.95±0.56
−0.2—0.0	28.5 ±0.71	11.09±1.21	14.04±1.30	12.61±0.89
0.0—0.2	26.8 ±0.69	26.05±1.86	25.23±1.74	25.57±1.27
0.2—0.4	14.0 ±0.50	48.33±2.53	44.15±2.30	46.05±1.70
0.4—0.6	6.04 ±0.33	72.14±3.09	57.95±2.64	64.57±2.02
0.6—0.8	4.05 ±0.27	72.37±3.10	53.32±2.54	62.26±1.98
0.8—1.0	2.92 ±0.23	49.74±2.57	40.56±2.21	44.85±1.68
1.0—1.2	3.37 ±0.25	27.83±1.92	24.19±1.71	25.87±1.28
1.2—1.4	3.32 ±0.24	17.60±1.53	18.29±1.49	17.93±1.07
1.4—1.6	2.81 ±0.24	12.15±1.27	12.86±1.25	12.50±0.89
1.6—1.8	2.42 ±0.21	8.83±1.09	8.63±1.02	8.70±0.74
1.8—2.0	2.03 ±0.19	8.04±1.04	8.27±1.00	8.14±0.72

TABLE IV. Cross sections $(d^2\sigma/dt\,dx)/\sigma_T$ [(GeV/c)$^{-2}$] for $\pi^-(\gamma)+p\to X+p$ at $t=-0.05$ (GeV/c)^2 and fits to the form $d^2\sigma/dt\,dx=[A/(1-x)+B(1-x)]e^{b(t+0.05)}$.

Beam particle	π^-	γ	γ	γ
Beam momentum (GeV/c)	100	75—100	100—148	75—148
σ_T	24.0 mb	115.9 μb	114.9 μb	115.3 μb
A/σ_T [(GeV/c)$^{-2}$]	0.118±0.006	0.130±0.009	0.111±0.007	0.122±0.006
B/σ_T [(GeV/c)$^{-2}$]	0.6±1.6	7.0±2.4	8.0±2.6	7.2±1.7
χ^2/DF (4 DF)	1.86	1.02	0.38	1.00
Range of $10^2(1-x)$	Cross sections			
2.0—2.5	5.93±0.42	5.89±0.53	4.92±0.46	5.37±0.39
2.5—3.1	4.56±0.34	4.63±0.43	4.24±0.39	4.42±0.29
3.1—3.9	3.23±0.25	4.42±0.37	3.76±0.32	4.07±0.24
3.9—4.9	2.56±0.20	3.37±0.29	2.73±0.25	3.03±0.19
4.9—6.1	2.01±0.16	2.43±0.23	2.41±0.21	2.42±0.15
6.1—7.7	1.60±0.13	2.39±0.20	2.27±0.18	2.32±0.13
7.7—9.6	1.60±0.12	2.17±0.18	1.94±0.16	2.05±0.12

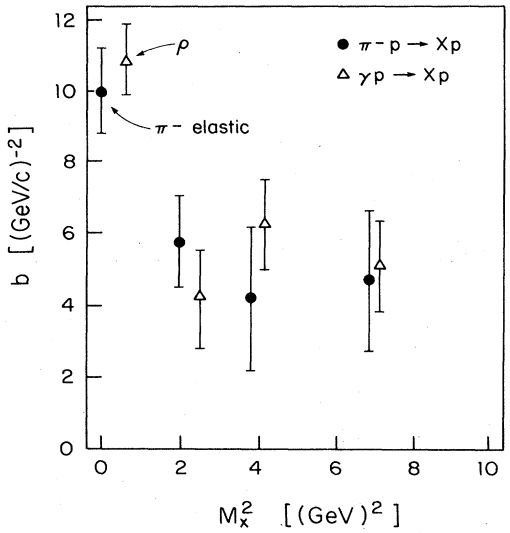

FIG. 9. The slope parameter b in the region $0.02 < |t| < 0.1$ $(\mathrm{GeV}/c)^2$ as a function of $M_X{}^2$ for $\pi^- p \to Xp$ at 100 GeV/c and $\gamma p \to Xp$ at 75–148 GeV/c.

presumed to be due to two photons produced in the radiator of which only one interacted in our apparatus. The energy resolution of the total absorption counter was not as good as that of the tagging system. Moreover, the tagging system resolution and efficiency deteriorated for photons below 75 GeV. For these regions we present in this paper only the data in the energy range 75–148 GeV.

A. Elastic cross sections

The elastic cross sections for $\pi^- p \to \pi^- p$ and $\gamma p \to \rho p$ are given in Table I. The data were fitted to the form

$$\frac{d\sigma}{dt} = Ae^{bt} \tag{7}$$

and normalized by adjusting the parameter A as explained in Sec. IV D. Figure 8 shows some t distributions. Slope-parameter values are plotted in Fig. 9. The photon elastic data contain about 6% ω and 4% ϕ signal. The effect of this contamination on the ρ slope is insignificant. However, the normalization of the inelastic data, as mentioned previously, was corrected accordingly. The pion slope of 9.9 ± 1.0 $(\mathrm{GeV}/c)^{-2}$ agrees, within errors, with the value of 8.92 ± 0.31 $(\mathrm{GeV}/c)^{-2}$ obtained in the Fermilab experiment E-396.[8] The ρ slope is about one unit larger than that of π^-. This difference can be understood in terms of the Drell[13] and Söding[14] mechanism which produces a nonresonant background in the vicinity of the ρ peak. The mass resolution of our experiment does not permit a direct determination of this background. However, a calculation using the fit parameters of Ref. 12 shows that the net result of this t-dependent effect is to increase the slope parameter by about one unit. Correcting for this effect changes the value of the ρ photoproduction slope from 10.6 ± 1.0 to 9.6 ± 1.0 $(\mathrm{GeV}/c)^{-2}$. The corrected value is then identical, within errors, to our π^- elastic-scattering slope, 9.9 ± 1.0 $(\mathrm{GeV}/c)^{-2}$, in agreement with the prediction on the VDM.

B. Inelastic cross sections

The inelastic cross sections for $\pi^-(\gamma) + p \to X + p$ as a function of $M_X{}^2$ and $1-x = (M_X{}^2 - M_0{}^2)/s$, where x is the Feynman variable and M_0 is the mass of the incident particle, are given in Tables II–IV. For each $M_X{}^2$ or $1-x$ bin, all data in the region $0.02 < |t| < 0.1$ $(\mathrm{GeV}/c)^2$ were used to calculate the value at $t = -0.05$ $(\mathrm{GeV}/c)^2$ for which the cross sections are presented. For a given s, there is, of course, a one to one correspondence between $1-x$ and $M_X{}^2$. However, in the case of the photon data a given $1-x$ value corresponds to different $M_X{}^2$ values depending on the energy of the photon within the energy bin. For this reason the data are given both in the $M_X{}^2$ and the $1-x$ representation. Since the extraction of elastic events, as discussed in Sec. IV C, can only be done in the $M_X{}^2$ representation, the cross sections $d\sigma/dx$ in Table IV are presented only for values of $1-x$ corresponding to $M_X{}^2 \geq 3$ GeV^2 (for the lowest value of the energy in the energy bin). On the other hand, since our efficiency deteriorates for $1-x > 0.1$, the upper value of $M_X{}^2$ in Table II corresponds to $1-x \sim 0.1$.

The t distributions for various $M_X{}^2$ intervals are given in Table I. Figure 9 shows the slope parameter b of the t distributions as a function of $M_X{}^2$. For $M_X{}^2 > 4$ GeV^2, the inelastic slopes are about one half of the elastic slopes and appear to be independent of $M_X{}^2$. With the exception of a small difference in the elastic slopes, which was explained above in terms of the Drell-Söding mechanism, the photon and pion slopes are the same, as expected by the VDM.

The mass distributions are plotted in Fig. 10(a). According to the simple VDM, photon dissociation proceeds via an intermediate vector meson ρ, ω, or ϕ. Since the ρ dominates, we will consider only the effect of the ρ in this discussion. The photoproduction of ρ mesons is considered, in the VDM, to represent "elastic scattering" of photons. Therefore, in order to compare photon data with pion data under the VDM, the mass distributions should be plotted against $M_X{}^2 - M_0{}^2$, where $M_0 = M_\pi$ or M_ρ for pion or photon data, respectively. Such a plot is presented in Fig. 10(b). Except for the difference in the widths of the elastic peaks, which is partly due to the natural width of the ρ and partly due to the slightly different resolutions of the two sets of data, the two spectra look identical. This confirms the prediction of the VDM.

The distributions in $1-x$ are particularly significant for diffractive processes.[2] For $\pi^-(\gamma) + p \to X + p$, the change in the mass of the incident particle requires a minimum momentum transfer to the target proton equal to

$$|t|_{\min}{}^{1/2} = M_p(1-x) = M_p \frac{M_X{}^2 - M_0{}^2}{s}, \tag{8}$$

where M_0 is the mass of the incident particle. The smaller the momentum transfer, the more coherently the reaction can proceed. Since the concepts of coherence and diffraction are closely related, it appears reasonable that

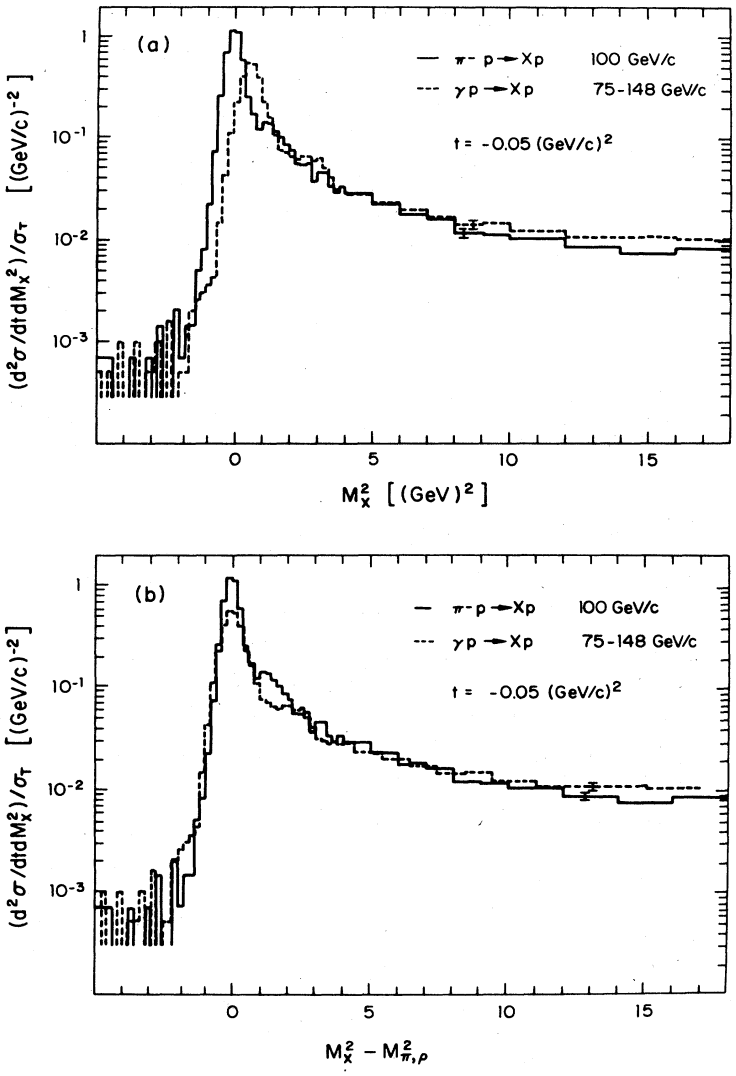

FIG. 10. Differential cross sections $d^2\sigma/dt\,dM_X^2$ at $t=-0.05$ (GeV/c)^2 for $\pi^- p \to Xp$ at 100 GeV/c and $\gamma p \to Xp$ at 75—148 GeV/c. The two distributions are normalized relative to each other by the corresponding total cross sections. Cross sections (a) plotted against M_X^2; (b) plotted against $M_X^2 - M_0^2$, where M_0 is the mass of the pion (ρ meson) for the π^- (γ) data.

different diffractive processes should be compared at the same $1-x$ rather than at the same M_X^2 values. Table IV and Fig. 11 present $1-x$ distributions for pion and photon data and fits to the form

$$\frac{d^2\sigma}{dt\,dx} = \left[\frac{A}{1-x} + B(1-x)\right] e^{b(t+0.05)} . \tag{9}$$

This fit is inspired by the triple-Regge model.[2] The form of the A term is predicted by the triple-Pomeron amplitude. In hadron dissociation, this term was found to scale to the total cross section of the dissociating hadron,[1] as predicted by factorization (see below). The B term, on the other hand, does not scale and, moreover, it was found to vary significantly from experiment to experiment. This term is presumed to arise from nondiffractive processes. The events from such processes are likely to have more large angle tracks emanating from the target in addition to the recoil proton and therefore are detected with different efficiency by different experiments. This experiment suppresses events with more than one large-angle track, which are the events that contribute to B. Since the efficiency of our apparatus for minimum ionizing tracks was set purposefully low to reduce accidentals (our fastest recoil protons were six times minimum ionizing), it is impossible to calculate our bias against events of the B type. We therefore attribute no physical significance to the B terms presented in Table IV other than that the photon data appear to have a larger-B term than the pion data. The value of A/σ_T of the pion data is in agreement with the value 0.113 ± 0.003 (GeV/c)$^{-2}$ found in a previous experiment.[1]

In the Regge model, under the assumption of factorization, the high-mass diffraction-dissociation cross section arising from a triple-Pomeron term can be written as

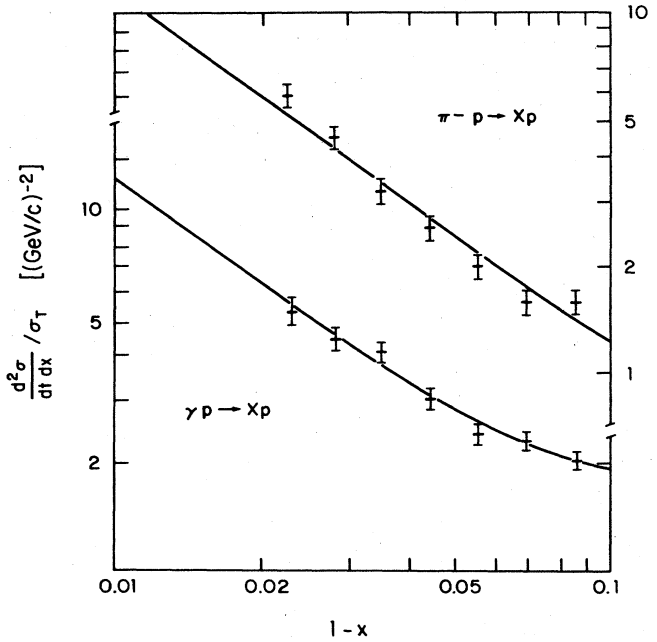

FIG. 11. Differential cross sections $(d\sigma^2/dt\,dx)/\sigma_T$ at $t=-0.05$ (GeV/c)^2 for $\pi^- p \to Xp$ at 100 GeV/c and $\gamma p \to Xp$ at 75—148 GeV/c. The curves represent fits to the form $d\sigma/dx = A/(1-x)+B(1-x)$.

$$\frac{d^2\sigma^{hp}}{dt\,dx} = \frac{\beta_{hP}(0)\beta_{pP}^2(t)G_{PPP}(t)}{16\pi(1-x)}\,, \tag{10}$$

where h represents a hadron dissociating on the proton, $hp \to Xp$, and P represents the Pomeron. In the same model, the total cross section at high energies is given by

$$\sigma_T^{hp} = \beta_{hP}(0)\beta_{pP}(0)\,. \tag{11}$$

In writing (10) and (11) we have taken, for simplicity, the Pomeron trajectory to be $\alpha(0)=1$ and, because of our small t values, the slope of the trajectory to be $\alpha'(t)=0$. The ratio of the diffractive to the total cross section,

$$\frac{d^2\sigma^{hp}/dt\,dx}{\sigma_T^{hp}} = \frac{\beta_{pP}^2(t)G_{PPP}(t)}{\beta_{pP}(0)16\pi(1-x)}\,, \tag{12}$$

is then independent of the incident-particle type. The $1/(1-x)$ behavior predicted by Eq. (10) and the scaling of the diffractive to the total cross section given by Eq. (12) have been found to hold for $\pi^\pm$, $K^\pm$, and $p^\pm$ hadrons dissociating on protons.[1] Since Eq. (9) fits the photon data satisfactorily, triple-Pomeron behavior is now also established for photons. The values of the A/σ_T terms of our pion and 75—148-GeV photon data are, respectively, 0.122 ± 0.006 and 0.118 ± 0.006. Thus, within the relative normalization uncertainty of $\pm16\%$, factorization is satisfied. These results indicate that the photon indeed behaves like a hadron despite the fact that its hadronic cross section is about 200 times smaller than that of the pion. In the VDM, it would be more appropriate to use $M_0=M_\rho$ in Eq. (8) which defines the variable $1-x$. Such a choice would change the value of A/σ_T of the photon data from 0.122 ± 0.006 to 0.110 ± 0.005. Within

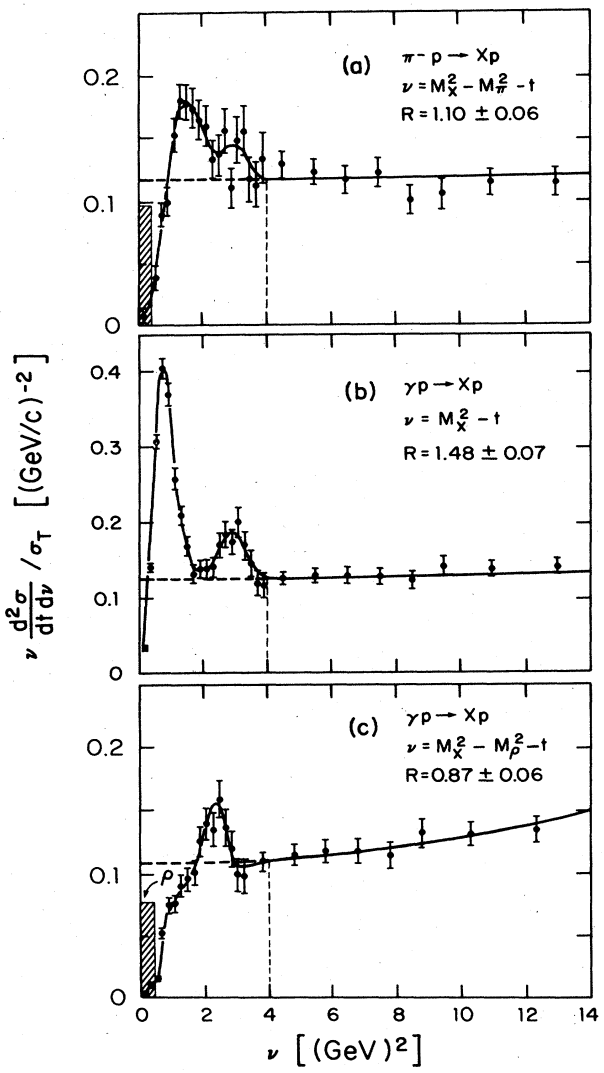

FIG. 12. Test of the finite-mass sum rule: The product $\nu(d^2\sigma/dt\,d\nu)/\sigma_T$ plotted against ν for $\pi^-(\gamma)+p \to X+p$ at $t=-0.05$ (GeV/c)^2. The variable ν is defined as $\nu=M_X^2-M_0^2-t$, where M_0 is the mass of the incident (dissociating) hadron. The solid curves represent proper fits to the data for $\nu>4$ GeV^2 and eyeball fits for $\nu<4$ GeV^2. The ratio R is defined by Eq. (14) in the text. (a) Pion data at 100 GeV/c (from Table II). The elastic contribution, $|t|(d\sigma/dt)/\sigma_T$, is represented by the hatched area. (b) Photon data at 75—148 GeV/c with $M_0=0$ (from Table III). (c) Photon data with the ρ peak subtracted (from Table II) and with $M_0=M_\rho$. As in the pion case, the "elastic" ρ contribution, $|t|(d\sigma/dt)/\sigma_T$, is shown pictorially as the hatched area.

errors, this last value is still in agreement with the value of the pion data. The test of factorization in our data cannot discriminate between the photon as an ordinary hadron and the prediction of the VDM.

The test of the finite-mass sum rule (FMSR), Eq. (3), is shown in Fig. 12. The term $|t|(d\sigma_{el}/dt)$ is simply a δ function at $\nu=|t|$. However, for presentation purposes, it is plotted as an area whose abscissa extends over a finite

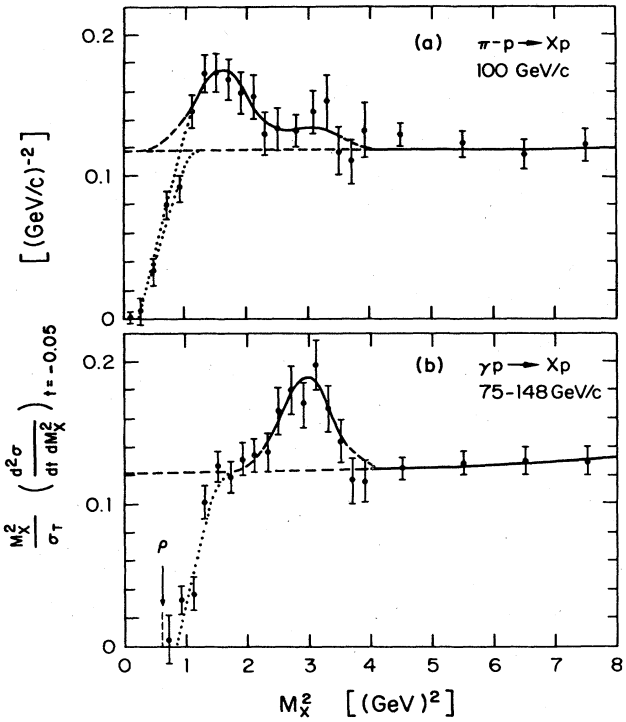

FIG. 13. Differential cross section $(M_X^2/\sigma_T)(d^2\sigma/dt\, dM_X^2)$ at $t=-0.05$ $(\mathrm{GeV}/c)^2$ for $\pi^- p \to Xp$ at 100 GeV/c and $\gamma p \to Xp$ at 75—148 GeV/c. The data, from Table II, do not include elastic $\pi^- p$ scattering and ρ photoproduction. The solid curves are fits to the data, the dashed ones represent extrapolations of the fits, and the dotted curves are drawn to guide the eye.

region of ν. The value of ν' was taken to be 4 GeV^2, safely above the "resonance region". The data for ν larger than ν' were fitted by using Eq. (9). The reader is reminded that the cross-symmetric variable ν is given by

$$\nu = M_X^2 - M_0^2 - t = (1-x)s - t \ . \tag{13}$$

The FMSR is tested by comparing the left-hand to the right-hand side of Eq. (3). Numerically, we evaluate the quantity

$$R = \frac{|t|\frac{d\sigma_{\mathrm{el}}}{dt} + \int_0^4 \nu \frac{d^2\sigma}{dt\, d\nu} d\nu}{\int_0^4 \nu \left[\frac{d^2\sigma}{dt\, d\nu}\right]_{\text{fit for } \nu>4} d\nu} \ . \tag{14}$$

A deviation of R from unity indicates violation of the FMSR. The sensitivity of the test increases as the value of the upper limit of integration, ν', decreases. However, ν' should not be allowed to fall into the low-mass resonance region. Our choice of $\nu'=4$ GeV^2 satisfies these criteria.

Figure 12(a) shows the pion data. We find $R_\pi = 1.10 \pm 0.06$. The photon data, for the energy bin 75—148 GeV, are shown in Figs. 12(b) and 12(c). In Fig. 12(b) we consider the photon to be the incident "hadron." Therefore, we set $M_0=0$ in Eq. (13), yielding $\nu = M_X^2 - t$, and find $R_\gamma = 1.48 \pm 0.07$. Clearly, in this straightforward application, the FMSR fails for the photon data. In Fig. 12(c), the incident (dissociating) hadron is considered to be the ρ meson and therefore M_0 is set equal to the mass of the ρ yielding $R_\rho = 0.87 \pm 0.06$. This value is in better agreement with unity than the value of R_γ. Thus, our results favor the VDM.

Actually, the value of R_ρ appears to be somewhat smaller than unity. Within the VDM, this could be caused by a "direct" dissociation of the incident photon, where the term "direct" means an interaction that does not proceed via an intermediate vector meson. Such an interaction has been proposed in order to explain the shadowing effects of photons incident on nuclear targets.[5] The direct interaction would produce an inelastic spectrum ν $(d^2\sigma/dt\, d\nu)$ in Fig. 12(b) which would be fairly flat in ν, similar to the pion inelastic spectrum of Fig. 12(a). Compton scattering, the elastic peak from such a direct interaction, was eliminated in our trigger. Assuming no interference between the direct and VDM amplitudes, the ratio of the direct to the VDM dissociation cross sections may be determined by subtracting a constant term from the cross sections in Fig. 12(b) and demanding that the remaining cross sections satisfy the FMSR according to the VDM. Following such a procedure, this ratio is found to be 0.33 ± 0.16. Assuming now that the direct and VDM diffractive cross sections scale to the corresponding total cross sections, our result may be interpreted as representing a measurement of the direct hadronic cross section of the photon. In terms of the total cross section σ_γ^T, the direct cross section is thus given by

$$\sigma_\gamma^D = (0.25 \pm 0.12)\sigma_\gamma^T \ . \tag{15}$$

This value is consistent with the fact that the simple VDM accounts for only $\sim 80\%$ of the total photon cross section.[5] Furthermore, since the direct cross section is not expected to exhibit shadowing effects in nuclei,[5] our result is also consistent with experiments on nuclear shadowing which indicate that $\sim 20\%$ of the photon cross section is not shadowed.[5]

C. Resonance structures

As seen in Fig. 12, both the pion and the photon cross sections exhibit resonancelike behavior in the region of $M_X^2 < 4$ GeV^2. In the pion case, enhancements can be seen in the vicinity of the $A_1(1270)$ and the $A_3(1680)$, while in the photon case only one enhancement is visible, in addition to the ρ, corresponding to the ρ' (1600).

In order to extract the masses, widths, and cross sections of these enhancements, it is necessary to know the shape of the background under the peaks. Figure 13 shows the inelastic (ρ removed) cross sections

$$M_X^2 (d^2\sigma/dt\, dM_X^2)/\sigma_T$$

at $t=-0.05$ $(\mathrm{GeV}/c)^2$. This figure differs from Fig. 12 in that M_X^2 is used instead of ν, resulting in very similar background shapes for the pion and photon data. In particular, the rise of the pion cross section from threshold is identical to that of the photon cross section, assuming

TABLE V. Parameters of resonance structures obtained by fits to the pion (A_1 and A_3) and photon (ρ') data.

Parameter \ Resonance structure	A_1 (1270)	A_3 (1680)	ρ' (1600)
M^2 (GeV^2)	1.44± 0.13	2.96± 0.34	2.88± 0.09
σ_{M^2} (GeV^2)	0.46± 0.17	0.46± 0.34	0.42± 0.10
M (MeV)	1200±54	1720±99	1697±27
$\frac{d\sigma}{dt}[t=-0.05$ (GeV/c)^2] [μb/(GeV/c)^2]	1060± 248	146±84	2.65± 0.39
b [(GeV/c)$^{-2}$]	13.7± 2.0	5.0± 1.2	5.3± 1.0
σ_T (μb)	153±37	38±23	0.66± 0.13

that the interacting photon has the mass of the ρ as expected by the simple VDM. The shoulder to the left of the prominent peak in the photon case indicates that the extrapolation of the high-mass data fit into the low-mass region is a good representation of the background down to $M_X{}^2 \simeq 1.5$ GeV^2. A similar extrapolation in the pion data should then represent the background correctly down to $M_X{}^2 \simeq 1.5 - M_\rho{}^2 = 0.9$ GeV^2. Therefore, the pion and photon data were fitted in the mass regions 1.0—3.6 and 2.2—3.6 GeV^2, respectively, using as background the extrapolations of the corresponding high-mass fits. Since the widths of the peaks are comparable to the $M_X{}^2$ experimental resolution of ±0.3 GeV^2, Gaussian functions were used to fit the data. The solid curves in Fig. 13 show the best fits obtained in this manner, multiplied by $M_X{}^2$. The parameters of the fits are given in Table V. The last two rows in the table present the b slopes and the total cross sections integrated over t, obtained by assuming the form $d\sigma/dt = Ae^{bt}$. The slopes were taken from Table I. For the A_1, we use the slope of 13.7±2.0 (GeV/c)$^{-2}$, which was obtained from events of charged multiplicity $n_c \neq 1$, mainly $n_c = 3$. For the A_3 and ρ', the slopes are the averages over the mass regions 1—5 and 2—5 GeV^2, respectively.

The masses of our enhancements are consistent with their nominal values, although our ρ' mass seems to be somewhat high. The widths, after unfolding the experimental resolution, are in the range of 300—400 MeV, in agreement with values measured previously in $\pi^- p$[15] and γp (Ref. 16) diffractive interactions. Finally, our measured inclusive cross sections are in the range expected from these previous measurements which were made in exclusive channels. In particular, the production cross section of the ρ' (1600) by 40-GeV photons, followed by its decay into its (dominant) channel of $\rho^0\pi^+\pi^-$, was measured to be[16] 0.54±0.17 μb. Considering the uncertainty in the branching ratio and the errors in the cross-section measurements, our value of 0.66±0.13 μb is not inconsistent with the above measurement. Although the accuracy of the data does not permit more definite quantitative conclusions to be drawn, the agreement with previous measurements is found to be satisfactory.

VI. CONCLUSION

The differential cross section for diffractive photon dissociation on hydrogen, $\gamma p \to Xp$, is dominated by a ρ peak and a high-mass continuum. The ρ peak is exponential in t and has a slope parameter approximately equal to that of $\pi^- p$ elastic scattering. The high-mass data are also exponential in t and have slope-parameter values close to those of $\pi^- p \to Xp$. The $M_X{}^2$ distribution, plotted against $M_X{}^2 - M_\rho{}^2$ and scaled to the total cross section, is very similar to that of π^- dissociation. At high masses, it has a dominant $1/M_X{}^2$ behavior, consistent with a large triple-Pomeron presence in the diffractive amplitude. The scaling of the photon and pion data to their corresponding total cross sections establishes factorization at the level of ±16%, limited by the uncertainty in the normalization of the data. Finally, the finite-mass sum rule fails in a straightforward application, but is approximately satisfied if the "incident hadron" is considered to be the ρ meson. These results confirm the validity of the simple VDM, according to which the dissociation proceeds through an intermediate ρ meson.

There may be, however, a small discrepancy from the predictions of the VDM. Namely, the FMSR does not appear to be satisfied completely with the ρ as the only "incident hadron." If it is assumed that this discrepancy is caused by a certain probability that the photon dissociates "directly" (not via a ρ meson) into hadrons, and the ratio of direct to VDM cross sections is adjusted to satisfy the FMSR, this ratio is found to be 0.33±0.16. The further assumption that the diffractive cross sections scale to the corresponding total cross sections yields the result that the direct hadronic cross section of the photon is 25±12% of the total. This number agrees with experiments on shadowing of photon cross sections on nuclei and with the fact that the simple VDM accounts for only ~80% of the photon total cross section.

ACKNOWLEDGMENTS

We wish to thank Fermilab for its assistance during the assembly and testing of our apparatus and the running of the experiment. We are indebted to Richard Heidecker for his help with the mechanical design and construction of the apparatus and to Donald Humbert for his assistance in the design and construction of the associated electronics. This research was supported in part by the U.S. Department of Energy.

*Present address: IBM, Thomas J. Watson Research Center, Yorktown Heights, NY 10598.

[1]R. L. Cool *et al.*, Phys. Rev. **47**, 701 (1981).
[2]K. Goulianos, Phys. Rep. **101**, 171 (1983).
[3]A. I. Sanda, Phys. Rev. D **6**, 280 (1972); M. B. Einhorn, J. Ellis, and J. Finkelstein, *ibid.* **5**, 2063 (1972).
[4]Y. Akimov *et al.*, Phys. Rev. D **14**, 3148 (1976).
[5]T. H. Bauer, D. Spital, D. R. Yennie, and F. M. Pipkin, Rev. Mod. Phys. **50**, 26 (1978).
[6]T. J. Chapin *et al.*, Nucl. Instrum. Methods **197**, 305 (1982).
[7]R. L. Cool *et al.*, Phys. Rev. Lett. **48**, 1451 (1982).
[8]R. L. Cool *et al.*, Phys. Rev. D **24**, 2821 (1981).
[9]Gregory Snow, Ph.D. thesis, The Rockefeller University.
[10]K. Goulianos *et al.*, Phys. Rev. Lett. **48**, 1454 (1982).
[11]S. Carroll *et al.*, Phys. Lett. **80B**, 423 (1979).
[12]P. Callahan *et al.* (unpublished).
[13]S. D. Drell, Phys. Rev. Lett. **5**, 278 (1960).
[14]P. Söding, Phys. Lett. **19**, 702 (1966).
[15]Yu. M. Antipov *et al.*, Nucl. Phys. **B63**, 153 (1973); C. Daum *et al.*, Phys. Lett. **89B**, 281 (1980); **89B**, 285 (1980).
[16]D. Aston *et al.*, Nucl. Phys. **B189**, 15 (1981).